Title
A study on the efficacy of flow mitigation devices in hard disk drives

Journal
IEEE Transactions on Magnetics, 42(6)

ISSN
0018-9464

Authors
Kirpekar, S
Bogy, D B

Publication Date
2006-06-01

Peer reviewed

A Study on the Efficacy of Flow Mitigation Devices in Hard Disk Drives

Sujit Kirpekar and David B. Bogy, *Fellow, IEEE*

University of California at Berkeley, Berkeley, CA 94720-1740 USA

We report on large eddy simulations of the turbulent flow of air in hard disk drives (HDDs) using a commercial CFD code. In particular, we focus on HDD casings in which flow-induced vibrations are reportedly reduced by small geometrical modifications. The modifications investigated are M1: a blocking plate situated between the disks, M2: a spoiler (or deflector) located behind (downstream of) the actuator arm, and M3: a similar deflector upstream of the arm. We observed that M1, M2, and M3 significantly modify the mean flow patterns in the drives. M1 reduces velocity magnitudes in most parts of the drive, the modification of M2 causes flow reversal in regions close to the hub, while M3 causes the shedding of vortices upstream of the actuator arm. Our analysis points to M1 as the best candidate for mitigating the effects of turbulent airflow. This is because M1 is more effective in reducing the root-mean-square velocity fluctuations near the suspension. M1 is also more effective in reducing the pressure fluctuations near the base-plate and suspension region. This reduction, however, is at the cost of approximately 20% higher windage. Finally, we note that M3 has the adverse effects of increasing velocity and pressure fluctuations and hence is not the ideal candidate for mitigating airflow effects, among the modifications considered here.

Index Terms—**Airflow, blocking plate, large eddy simulation, spoiler.**

I. Introduction

THE turbulent flow of air generated by spinning disks in hard disk drives (HDDs) is known to be major contributor to undesirable vibrations of the head stack assembly (HSA). The continuing demand for higher capacities in HDDs has resulted in a continual increase in areal densities. Densities in excess of 100 Gb/in^2 have been demonstrated and it is widely projected that conventional technology will ultimately achieve 1 Tb/in^2. It is foreseeable that at such areal densities, a track density of 0.5 million tracks/inch will be required, with each recorded bit being roughly 13×50 nm [1]. Under such conditions, the tracking accuracy required is approximately 1.5 nm root mean square (RMS). These goals place stringent requirements on the positioning accuracy of the actuator while accentuating the need to mitigate the various sources of track misregistration (TMR).

Several methods/techniques have been proposed to tackle the TMR problem.

1) By reducing the disk diameter and increasing its thickness, which increases the rigidity of the disk, reducing the TMR caused by disk vibrations and spindle run-out.
2) By increasing the stiffness of the HSA, especially the suspension. This causes the modes of vibration to move to higher frequency ranges, thereby reducing their relative amplitudes.
3) By achieving better control using a dual stage actuator.
4) By isolating the drive from external vibration, using fluid spindle bearings and possibly replacing the air with a lower density, noncorrosive gas like helium [1].
5) By modifying the air flow in the drive using geometrical features, such that the resultant HSA vibrations are reduced.

The specific goals of this work are: 1) to describe and understand the mechanics of flow in hard disk drives with such flow-mitigating modifications using numerical simulation; 2) to quantify the effect of each modification on the RMS fluctuations; and 3) to provide a direct comparison of the performance of such modifications to aid future work in reducing flow-induced vibrations.

The modifications studied herein are in current use in disk drives and have been selected for investigation after examining several disk drives available in the market, in late 2004. The modifications investigated are: M1: a blocking plate situated between the disks, M2: a spoiler (or deflector) located behind (downstream of) the actuator arm, and M3: a similar deflector upstream of the arm. A comparison is made between the modifications M1-3 and the original disk drive without any modification, which we denote as M0.

This paper is organized into three parts.

1) In Part I, we review the literature on the problem of air flow effects in disk drives, both experimental and numerical. Next we describe the geometric details of the modifications and outline the simulation techniques we used.
2) In Part II, we discuss the major flow features associated with each modification with a view to understand the underlying physics. We report on how the flow develops after formation of the wake and how the turbulence intensity varies across the drive enclosure.
3) In Part III, we present velocities and pressure data in the immediate vicinity of the actuator arm. Here, we present RMS fluctuations and their corresponding frequency content.

II. Part I

A. Prior Research

There has been significant experimental, theoretical and numerical research on air flow in hard disk drives, over the past 30 years. A comprehensive review of the literature is detailed in the Ph.D. thesis of [2], but this may not be available to all readers. Hence, we provide a short review of the main accomplishments so far.

Digital Object Identifier 10.1109/TMAG.2006.873193

Experimental Research: The experimental work of Lennemann [3] was one of the first experimental investigations directly focused on disk drives. The author used model disks of diameter between 355.6 and 457 mm running at 710–600 rpm and used water and aluminum powder for flow visualization. Experiments were performed with and without a slider arm. The author shows the existence of a central laminar core that is rotating slightly slower than the disk and a highly turbulent outer region. The paper also contains an extensive list of prior work related to rotating disks, but not specifically disk drives.

Kaneko *et al.* [4] performed similar flow visualization experiments to study the flow between disks with and without a cylindrical shroud. They observed a "bumpy laminar core" that extended from the hub to the mid-radius of the disks, followed by a "more turbulent outer region."

Abrahamson *et al.* [5] performed experiments using an acid-base indicator, Bromothymol Blue, in water. Disk speeds were varied from 5 to 50 rpm, the disk diameter was fixed at 112 cm. They observed three distinct regions of flow: "a solid body inner region near the hub, an outer region dominated by counter rotating vortices and a boundary layer region near the shroud." They reported that decreasing the Ekman number $(Ek = \nu/R^2\Omega)$ or increasing the axial spacing between the disks resulted in lesser vortical structures in the outer region and consequently greater overall mixing.

Girard *et al.* [6] investigated the effect of an actuator-like rotary arm on the flow field in the drive, using water based flow visualization. Their main conclusions were related to the effect of the arm and the wake it creates.

Several authors [7]–[9] performed several laser-Doppler velocimetry experiments of rotating disks with and without an obstruction. They primarily reported mean and RMS values of circumferential velocities and the corresponding frequency content. Usry *et al.* [9] also conclude that once the flow separates by flowing over the obstruction, "the flow does not recover within one revolution from the effects of the obstruction."

Experimental research using realistic disk drive configurations for suspensions and sliders has been limited. Yamaguchi *et al.* [10] performed hot wire anemometer experiments using a suspension in a uniform and rotating flow. They found no noticeable peaks in the frequency content of the flow and concluded that the flow acts as an aperiodic irregular excitation.

In the Ph.D. thesis of Gross [11], experimental data in the near vicinity of the e-block arm was made available. Gross also investigated the effect of the thickness of the e-block arm and the shape of its trailing edge on the airflow and consequently on the flow induced vibrations in the slider.

Numerical Research: Among the first numerical investigations of the air flow in disk drive like enclosures was done by Chang *et al.* [12]. Using a finite difference code incorporating the $k-\epsilon$ model, they showed good agreement between experiments and simulation with regard to the mean flow velocity and heat transfer characteristics.

The first three-dimensional numerical study of the *unsteady* flow was published by Humphrey *et al.* [13]. They showed that the toroidal vortices at the shroud "acquire a time-varying sinuous shape in the circumferential direction."

Using a different code, Suzuki *et al.* [14] numerically studied the effect of a radially inserted actuator arm and an "airlock" (which is a similar obstruction to the flow). They mainly discuss the pressure, shear stress and disk torque coefficient that they compute. Using the same code as Suzuki *et al.* [14], Iglesias *et al.* [15] performed two- and three-dimensional calculations for different Reynolds numbers. Using a similar noncommercial software Kazemi [2] has conducted 2-D and 3-D numerical calculations of the flow around a suspension-head unit and reports the resulting vibrations calculated by a finite-element technique.

Most of the recent works on air flows in disk drives have used commercial CFD software. Due to the rapid increase in computer speeds and research advances in turbulence modeling, numerical investigations are increasingly modeling the geometrical complexities of a real HDD.

Ng *et al.* [16] performed CFD calculations using CFX-5, Shimizu *et al.* [17] used large eddy simulation (LES) to study flow induced disk flutter, and Shimizu *et al.* used LES to study the airflow induced vibrations of the HGA. Tsuda *et al.* [18] report DNS results, while Tatewaki *et al.* [19] report LES results of airflows in realistic disk drives.

Recognizing that the air flow in a disk drive is highly unsteady and random, most researchers have performed unsteady (time-marching) calculations, typically using LES, (or where resources permit, DNS). Calculations based on Reynolds Averaged methods (which are useful in predicting mean flow fields and particle trajectories) have also been reported by Song *et al.* [20].

Finally, there has also been some published work on reducing flow induced vibrations in disk drives. Hirono *et al.* [21] study the effect of an upstream spoiler, while Nakamura *et al.* [22] study the effect of miniaturizing the suspension. There has also been some (experimental) work using very similar modifications that have been studied here. For example, Deeyienyang *et al.* [23] studied the use of "squeeze air bearing plates" in reducing the vibrations of the disk. Other methods of mitigating flow induced vibrations have also been proposed. For example, Hendriks *et al.* [24] propose the use of an "aerodynamic bypass" which can offer drastic reduction in the upstream pressure at lower costs.

B. Model Setup

A top view of the geometrical models simulated are shown as follows, M0 in Fig. 1, M1 in Fig. 2, M2 in Fig. 3, and M3 in Fig. 4.

The relevant geometrical modifications have been highlighted for clarity. Geometrical data that is common to all simulations is given in Table I, while geometrical data specific to each simulation is given in Tables II–IV. Numerical modeling information that is common to all simulations is given in Table V and boundary conditions are outlined in Table VI. Our simulations use the Algebraic dynamic LES model [25] which the authors consider to be the optimal LES model for the current work (see [26]). To avoid the well known diffusive behavior of upwind based methods with LES [27], we use central differencing for discretizing the convective terms. A time step of 2×10^{-5} s was chosen so that we are able to resolve a maximum frequency of 25 kHz. A steady $k-\epsilon$ solution was used as initial conditions

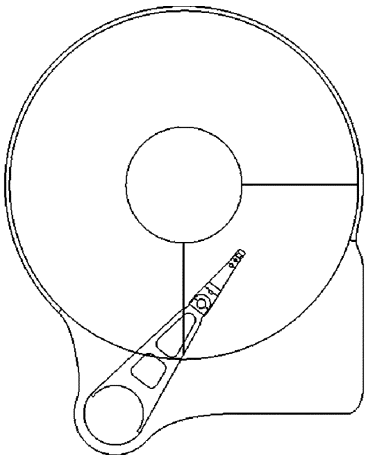

Fig. 1. Top view of M0 geometry: original simulation.

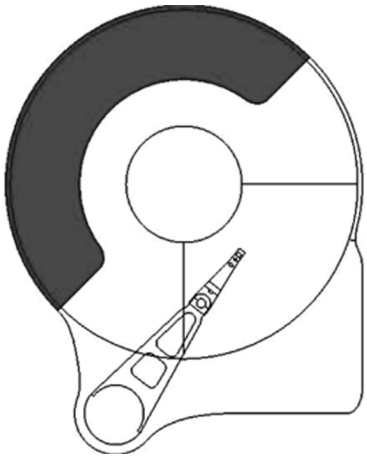

Fig. 2. Top view of M1 geometry: blocking plate.

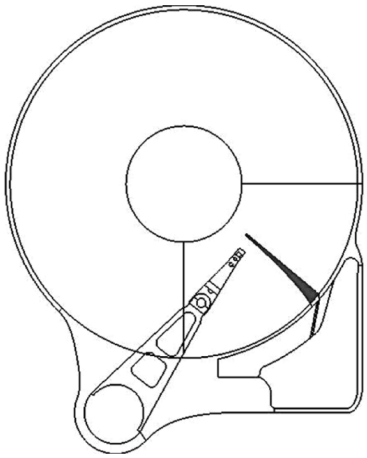

Fig. 3. Top view of M2 geometry: downstream spoiler.

for all of the simulations. Such a steady $k-\epsilon$ solution forms a good equilibrium approximation to the mean flow from which the transient solutions can be computed.

Finally, information about the mesh used in the simulations is given in Table VII. All simulations used an unstructured mesh that was created in 2-D and extruded in the axial direction. The mesh generation algorithm creates a grid which is dominant in

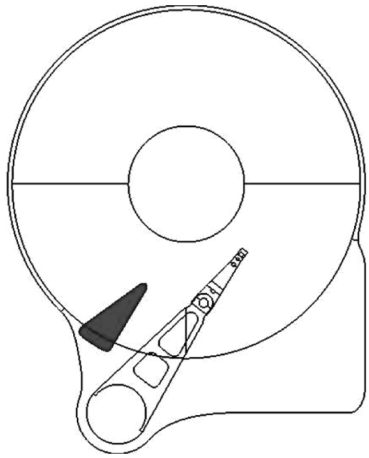

Fig. 4. Top view of M3 geometry: upstream spoiler.

TABLE I
GEOMETRY DATA

Number of disks	2
Number of e-block arms	1
Number of base plates	2
Number of suspensions	2
Number of sliders	2
Spacing between disks (mm)	2.2
Disk diameter (mm)	76.2
Width of shroud gap (mm)	1
Length of actuator (mm)	45
Length of e-block arm (mm)	32.5
Length of base plate (mm)	6.5
Length of suspension (mm)	11.1
Thickness of e-block arm (mm)	0.8
Thickness of base plate (mm)	0.3
Thickness of suspension (mm)	0.1
Dimensions of slider (mm)	$1 \times 0.8 \times 0.3$
Number of weight saving holes in e-block arm	2

TABLE II
MODEL SPECIFIC GEOMETRY DATA, M1

Thickness of blocking plate (mm)	0.8
Angular dimension of blocking plate (degrees)	180
Radial dimension of blocking plate (mm)	16.25

TABLE III
MODEL SPECIFIC GEOMETRY DATA, M2

Thickness of downstream spoiler (mm)	1.6
Maximum width of downstream spoiler (mm)	2.65
Length of downstream spoiler (mm)	20.75

TABLE IV
MODEL SPECIFIC GEOMETRY DATA, M3

Thickness of upstream spoiler (mm)	1.4
Maximum width of upstream spoiler (mm)	8
Length of upstream spoiler (mm)	17.5

quadrilateral cells, with approximately 90% of the cells being quadrilateral, the rest being triangular. This helps in two ways: more grid lines (i.e., cell faces) can be oriented orthogonal to the direction of the mean flow, and the total number of cells for a given maximum cell width is reduced, compared with a purely

TABLE V
CFD MODELING INFORMATION

Governing equations	Filtered Navier Stokes equations
Solution algorithm	SIMPLEC [28]
Large eddy simulation model	Algebraic dynamic [25]
Type of LES filter	Top-hat (variable width)
Temporal differencing scheme	Crank Nicholson (second order)
Spatial differencing scheme (convective term)	Central differencing
Time step (seconds)	2.0×10^{-5}
Number of time steps	2400
Corresponding disk rotations	8
Initial conditions	Steady k-ϵ solution

TABLE VI
BOUNDARY CONDITIONS

Disks	Rigid rotating walls, no slip
Shroud	Rigid wall, no slip
Shroud gap	Axial symmetry (zero normal gradient)
Other top and bottom surfaces of computational volume	Axial symmetry (zero normal gradient)
Hub/base of e-block arm	Fixed (similar to a cantilever)
Slider-disk interface	Slider slips on disk No cells between slider and disk
All structural interfaces (e.g. suspension+slider, e-block arm+base plate)	Rigidly joined (i.e. no dimple)
All fluid-structure surfaces	walls, no slip

TABLE VII
GRID INFORMATION

	M0	M1	M2	M3
Type of mesh	unstructured, hexahedral	←	←	←
Number of vols.	1,025,772	872,284	890,532	895,769
Max. vol. ($mm^3 \times 10^{-2}$)	8.996	9.521	9.436	9.390
Min. vol. ($mm^3 \times 10^{-5}$)	3.433	3.315	5.836	6.855
Avg. vol. ($mm^3 \times 10^{-2}$)	1.179	1.243	1.442	1.571
Avg. res. (mm)	0.2276	0.2316	0.2434	0.2504
Number of axial cells	32	32	32	32

triangular mesh. The mesh used for the simulation M0 is shown in Fig. 5, where the grid lines are plotted on the midplane between the disks. The grid is nonuniform, and a significant portion of the grid nodes are concentrated in the vicinity of the actuator and in it's wake. The resolution is also increased near the shroud and the disks. Thirty-two cells were used (totally) in the axial direction. While it is known that the axial resolution greatly affects the shedding dynamics, our resolution was chosen for computational feasibility. Nonetheless, the limited axial resolution has the possibility of affecting all the unsteady results and should be investigated on the availability of more computational resources.

In Table VII the average cell volume is calculated by taking a mean of all the computational volumes in the simulation domain. The average grid resolution is the cube root of the average cell volume, which forms a measure of the representative grid size. We note that the grid resolution used in our studies is at the limit of current desktop computers. Each of our calculations takes several (3–4) weeks to complete, hence performing such calculations for different grids and observing the convergence of statistical quantities is not feasible. However, an estimate of the grid resolution may be got by comparing our grid size with the

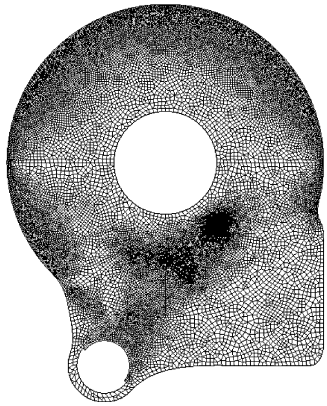

Fig. 5. Unstructured grid displayed on the midplane between the disks: M0.

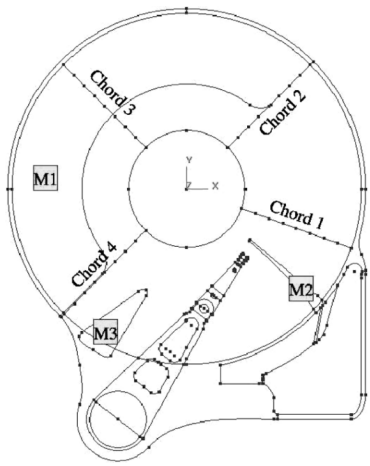

Fig. 6. Chord locations for calculation of turbulence intensity.

Kolmogorov scale for such flows [2], [26]. This comparison tells us that our resolution is approximately 15× the Kolmogorov scale of the flow, which suggests that our grid resolution is appropriate for large eddy simulation.

III. PART II

We start by discussing some physical features of the flow and subsequently describe the more quantitative results.

A. Major Flow Features

Flows in disk drive enclosures are highly unsteady with partly laminar and partly turbulent regions. Snapshots of the turbulent flow in our simulations are shown in Figs. 7–10. Plotted therein is the axial component of velocity on the midplane between the disks. Instead of choosing a monotonic scale for plotting this component of velocity, a staggered scale (similar to an interference pattern) is used. This helps in visualizing sharp velocity gradients that characterize the turbulent eddies, which may not appear in a monotonic scale. However quantitative information about the velocity magnitude is lost in this presentation mode. Nonetheless, this is acceptable for now, since we refer to quantitative data in later sections.

As the air flows over the structures forming an obstruction, it undergoes separation causing the formation of vortical structures (see (1) in Fig. 7). The vortex shedding causes changes

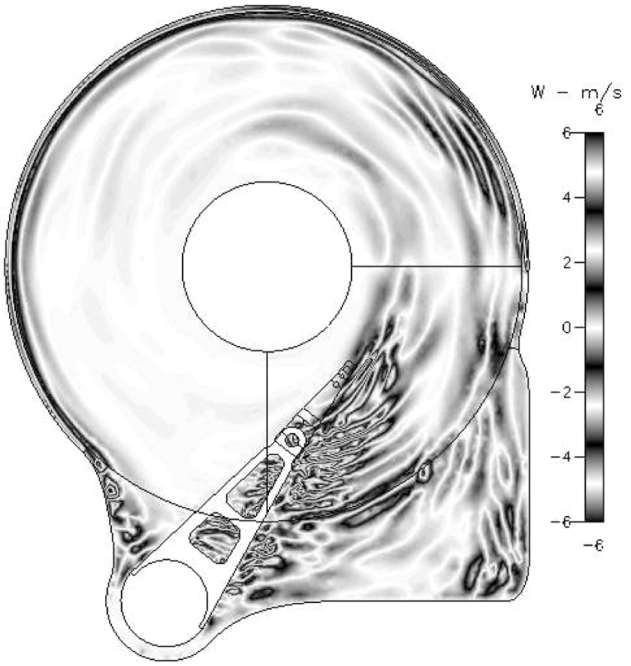

Fig. 7. M0: Snapshot of turbulent field in the drive. Plot of axial velocity component on the midplane.

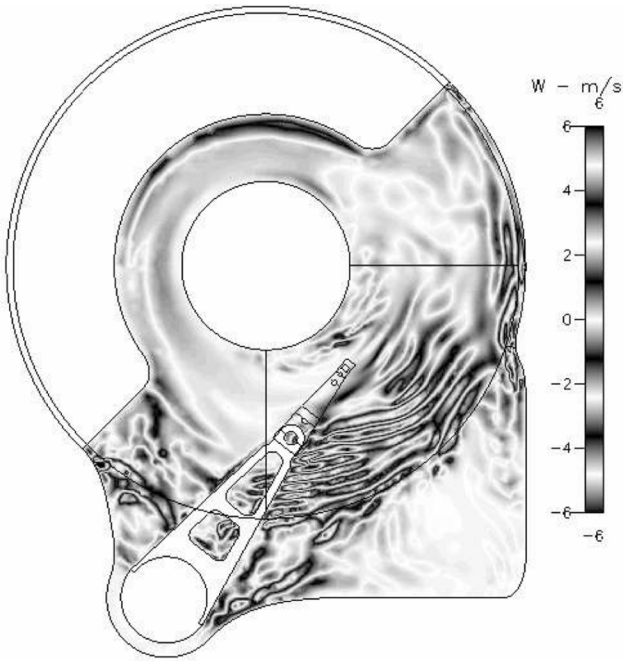

Fig. 8. M1: Snapshot of turbulent field in the drive. Plot of axial velocity component on the midplane.

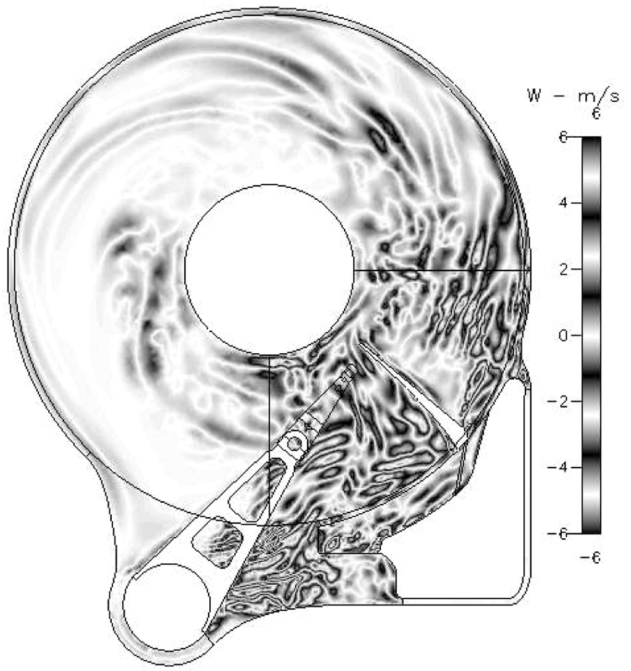

Fig. 9. M2: Snapshot of turbulent field in the drive. Plot of axial velocity component on the midplane.

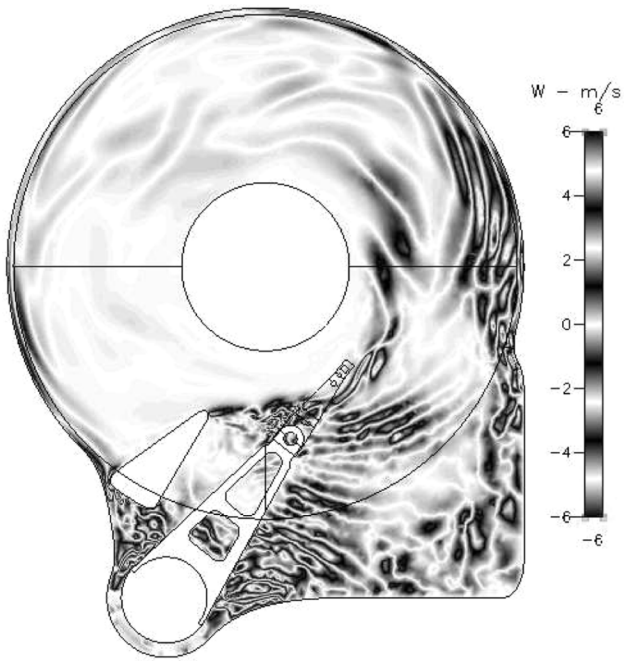

Fig. 10. M3: Snapshot of turbulent field in the drive. Plot of axial velocity component on the midplane.

in the circulation around the arm, which causes fluctuation in the drag it experiences. Turbulent eddies formed in the wake of the arm are convected by the mean flow due to the disk rotation and dissipate by the time they reach an angular position of approximately 225° (see (2) in Fig. 7). In describing radial and angular locations of our geometry, the origin is taken at the center of rotation of the disks. Angular positions are calculated by counter-clockwise rotation from the horizontal axis.

This dissipation is due to viscous action and converts the kinetic energy of the turbulent flow to internal energy. The turbulence intensity of the flow coming toward the actuator arm is between 5% and 10% (as later explained by Fig. 19). At the curved wall which forms the shroud one observes the presence of one or two toroidal vortices (see (3) in Fig. 7). These structures appear to be Taylor vortices formed due to three dimensional instability of the laminar boundary layer as it flows over

the concave boundary. Finally, in the region upstream of the actuator arm, where the enclosure expands to accommodate the arm, one observes the separation of the flow and the formation of a turbulent region. (see (4) in Fig. 7)

When compared with M0, M1 shows significant changes in the flow field, which is plotted in Fig. 8. The presence of the blocking plate essentially blocks out a significant portion of the flow, forcing the rest around it. The mean velocity of the flow is reduced because the blocking plate acts in regions where the linear velocity of the disk is higher. However, vorticity shedding at the trailing edge of the blocking plate increases the turbulence of the flow approaching the e-block arm (see (5) in Fig. 8). Also, one observes the presence of a region of flow reversal (and stagnation) near the hub. The presence of the blocking plate causes an adverse pressure gradient in the air flowing toward it, causing some portions of the flow to stagnate and reverse direction (see (6) in Fig. 8).

In simulation M2, plotted in Fig. 9, the presence of a thick (1.6 mm compared to a disk-to-disk spacing of 2.2 mm) downstream rib blocks a significant portion of the flow. At the midplane, the mean azimuthal velocity is decreased almost everywhere in the drive. The presence of the rib causes the flow to stagnate and reverse direction in a significant portion of the drive (see (7) in Fig. 9). The inner and outer edges of the rib are a source of vorticity shedding too, which increases the turbulence intensity of the downstream flow (see (8) in Fig. 10).

In simulation M3, which is plotted in Fig. 10, the flow field is similar to M0, except that the upstream spoiler acts as another source of generation of turbulent eddies. The eddies shed from the top and bottom edges cause added velocity fluctuations in the upstream portion of the flow field (see (9) in Fig. 10). This significantly increases the velocity fluctuations near base of the e-block arm and the suspension.

B. Evolution of Flow

It is expected that the airflow velocity magnitude is the smallest in the wake, and the flow gains momentum from the rotating disks as it flows around. To gain more insight into this process we plot the inter-disk velocity profiles at four points in the drive. In polar $(r(\mathrm{mm}), \phi^\circ)$ coordinates, these four points are (14.96, 340°), (14.96, 45°), (14.96, 135°), (14.96, 225°). $r = 14.96$ mm corresponds to $1/3$rd the radial span of the disks, chosen so as to not lie within the blocking plate. The angular positions were chosen so as to not lie in the path of any modification. These angular locations are referenced using a right hand coordinate system. The origin lies at the center of the disks, and $\phi = 0$ corresponds to the horizontal passing through the origin. Angular positions are then increasing in the counter-clockwise direction. Data plotted in each figure is the average velocity profile over six revolutions of the disks. In this paper, when a direct comparison between simulations is permitted, the results are plotted using a common convention. This convention is explained in the legend given in Table VIII.

In Figs. 11–14, the azimuthal velocity of the flow is plotted as a function of the axial z coordinate for the above mentioned four points. $z = 0$ refers to the top of the bottom disk, while $z = 2.2$ mm refers to the bottom of the top disk. All figures are plotted to the same scale for convenience.

TABLE VIII
COMMON LEGEND FOR FIGURES IN THE PAPER

M0	Full Line	Original Simulation
M1	Dashed Line	Blocking Plate
M2	Dotted Line	Downstream Spoiler
M3	Dash-Dotted Line	Upstream Spoiler

It is observed that, at 340°, in the wake, M0 shows the *fullest* velocity profile, implying that the unmodified flow is the fastest in the wake. The velocity profile for M1 is less *full* because of the presence of the blocking plate, while M2 shows a midspan flow reversal in the wake. The presence of the downstream rib and its corresponding pressure gradient causes the flow to reverse directions in the wake. At any given instant we expect the air to flow both forward and backward, but when averaged over time, it appears that the mean flow is in the reverse direction. Our simulation shows that part of the flow closer to the disks flows in the direction of rotation, while the bulk of the center section flows in the reverse direction.

As the flow moves on to 45°, the velocity profiles for all the simulations become *fuller* due to the diffusion of momentum from the rotating disks. M0, which is the flow without any obstructions, shows the largest magnitude, while M2 shows the smallest profile. None of the profiles show flow reversal. The width of the (laminar) boundary layer is approximately the same in each simulation. M2 shows the largest velocity gradient in the boundary layer, hence we can expect higher viscous action at the disks. We also note that when averaged over time, the calculated velocity profiles are symmetric with respect to the midplane, as expected.

At 135°, M0 again shows the fullest profile, and M2 begins to show flow reversal, which is due to the presence of the downstream spoiler, approximately 180° upstream of this location. The profile for M3 is similar to M0, reduced in magnitude by approximately 50%. This is a direct consequence of the upstream spoiler.

Finally at 225°, the profiles for M0 and M1 are almost identical, M3 is reduced from M0 by approximately 50%, while M2 shows flow reversal. This confirms the fact that the presence of the downstream spoiler causes a significant portion of the flow in the drive to reverse direction, mostly in the regions close to the hub.

Figs. 15–18 show the radial velocity as a function of the axial coordinate for the same four points as in Figs. 11–14. In each figure, one observes a positive spike in radial velocity immediately adjacent to the disks, as expected, due to the centrifugal effect.

At 340°, in the wake, the radial velocity profiles are not too different from each other. They are mainly affected by the constraining geometry of the model, which tends to squeeze the flow in the radial space between the hub and the shroud. For this reason, two peaks in the radial inflow velocity (i.e., negative radial velocity) are observed for each profile.

At 45°, (see Fig. 17) the radial velocity of M1 is strongly negative. This is because the blocking plate tends to bend the streamlines toward the hub. The other profiles show radial outflow, with M2 showing the largest variation across the inter-disk spacing.

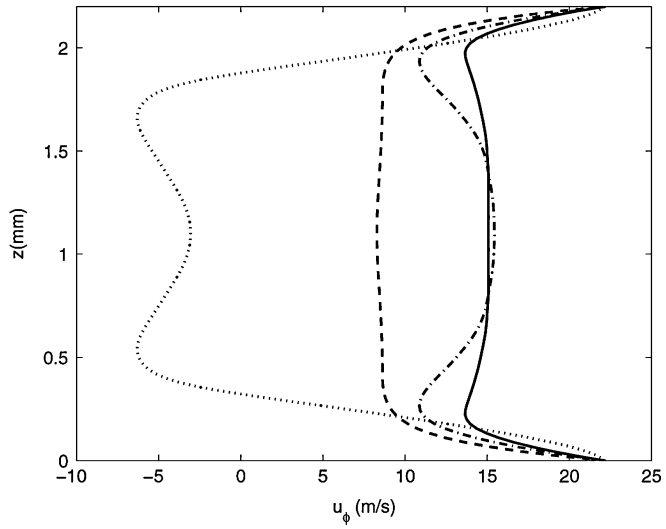

Fig. 11. Inter-disk azimuthal velocity profile, at 340° from origin, i.e., in the wake. (See Table VIII for legend.)

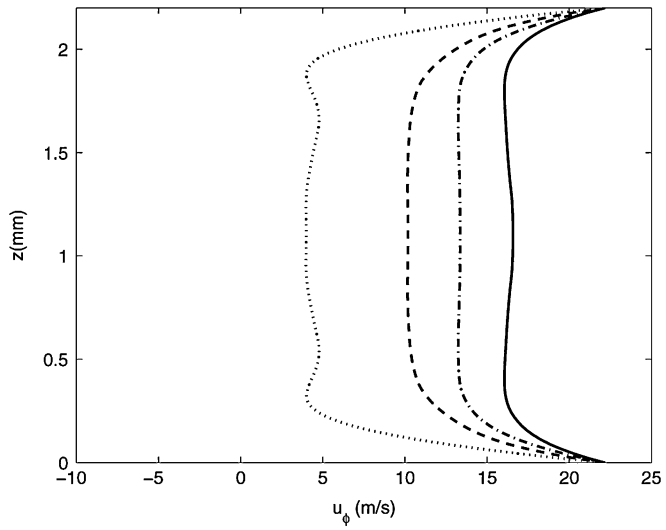

Fig. 12. Inter-disk azimuthal velocity profile, at 45° from origin. (See Table VIII for legend.)

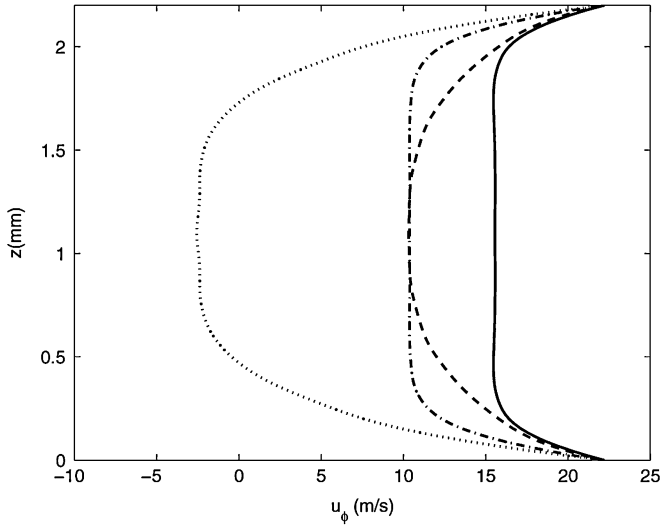

Fig. 13. Inter-disk azimuthal velocity profile, at 135° from origin. (See Table VIII for legend.)

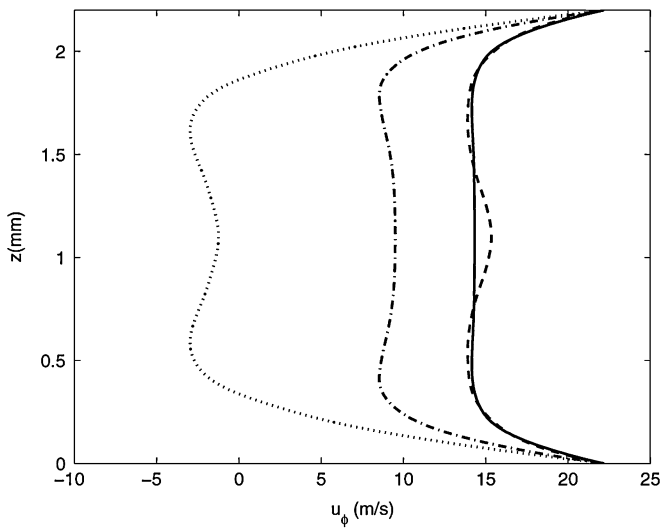

Fig. 14. Inter-disk azimuthal velocity profile, at 225° from origin. (See Table VIII for legend.)

At 135°, M1 again shows the effect of the blocking plate, while M3 shows the effect of the upstream spoiler, both of which tend to create radial inflows.

Finally, at 225°, the presence of the upstream spoiler is clearly evident as indicated by the strong negative radial velocity profile for M3. On the other hand, M1 now shows larger positive radial velocity, since beyond the trailing edge of the blocking plate lies an expansion region where the flow can radially spread, before approaching the actuator.

C. Turbulence Intensity

Fig. 6 shows a schematic diagram of the disk drive enclosure with all three modifications super-imposed. Also shown in this figure are four chords running from the inner radius to the outer radius at angular positions of 340°: Chord 1; 45°: Chord 2; 135°: Chord 3 and 225°: Chord 4. Plotted in Figs. 19–22 are the turbulence intensity (TI) profiles along these chords. The chord length is nondimensionalized by the radial span of the disks. Turbulence intensity is defined as the ratio of the RMS of (total) velocity fluctuation to the mean velocity at that location. In general, one observes that the TI is higher in regions closer to the hub, than regions near the outer radius. This is because, near the hub, the disk velocities are small, the flow tends to reverse direction and hence the RMS fluctuations appear to be a larger fraction of the mean.

For chord 1 in Fig. 19, one can clearly observe a single peak in TI due to the wake of the actuator arm for M0, M1, and M3. TI values are smaller near the outer and inner radii, hence it appears that a large part of the wake fluctuation is located near midway between the outer and inner radii. Compared to M0, M1 shows significantly reduced turbulence intensity. For M2 one observes two peaks, which is due to the vortex shedding occurring from the inner and outer edges of the downstream spoiler.

On observing the turbulence intensity of M1 in Figs. 20–22 we notice higher fluctuations near the hub at 45° and 135°, but higher fluctuations away from the hub at 225°. This is because

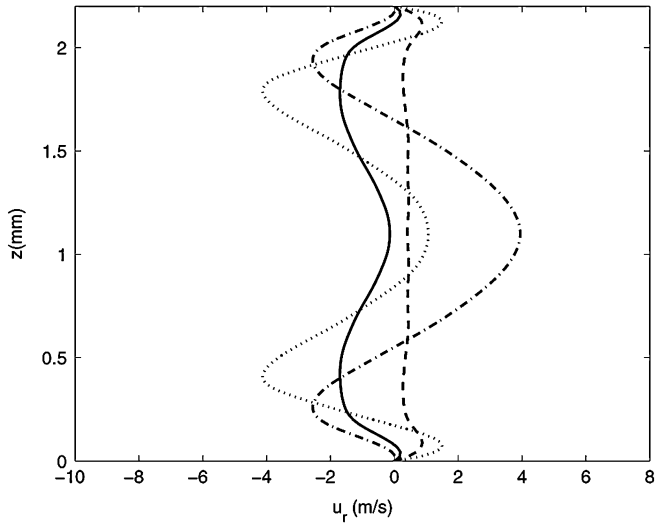

Fig. 15. Inter-disk radial velocity profile, at 340° from origin, i.e., in the wake. (See Table VIII for legend.)

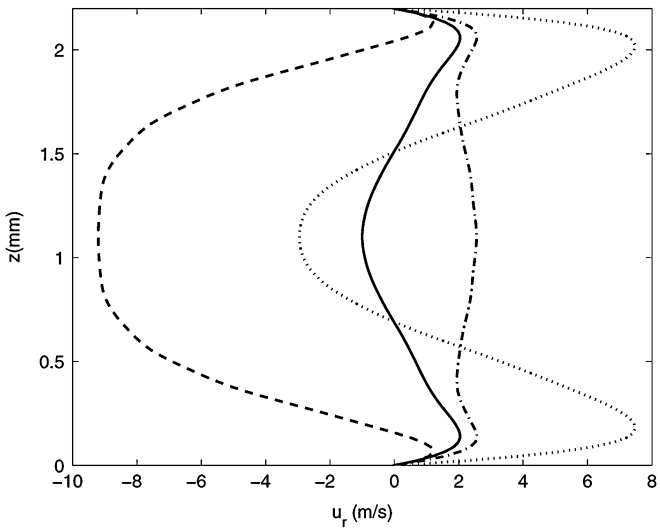

Fig. 16. Inter-disk radial velocity profile, at 45° from origin. (See Table VIII for legend.)

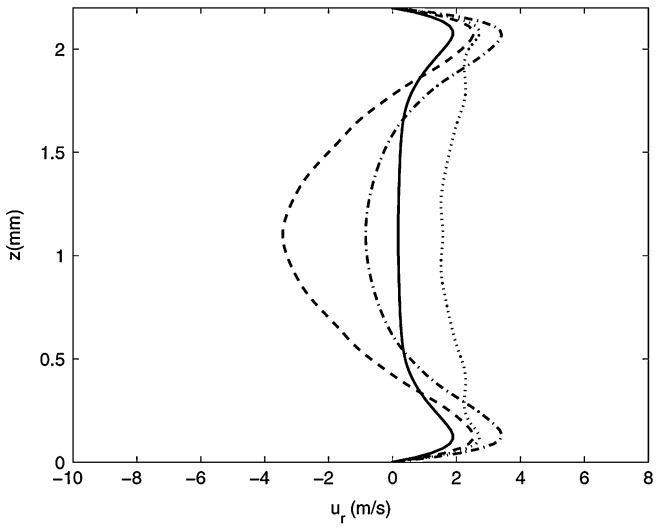

Fig. 17. Inter-disk radial velocity profile, at 135° from origin. (See Table VIII for legend.)

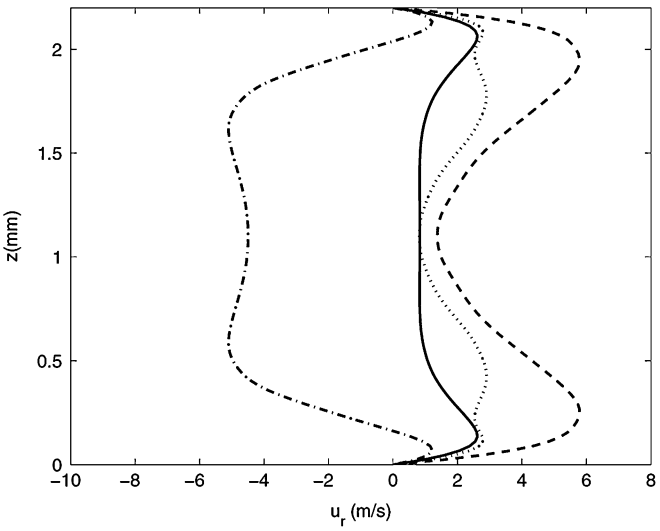

Fig. 18. Inter-disk radial velocity profile, at 225° from origin. (See Table VIII for legend.)

the vorticity shedding from the trailing edge of the blocking plate contributes to the fluctuations at 225°. (In Fig. 21, the TI profile for M1 is incomplete due to the blocking plate.)

M0 and M3 show remarkably similar TI profiles along each chord, indicating the presence of the upstream spoiler does not change the turbulent fluctuations along the chords being considered.

The TI profile for M2 along chord 4 (at 225°) shows a large peak approximately midway between the inner and outer radii. The presence of a large peak in TI implies that the flow is changing direction frequently, which makes the fluctuations a large percent of the mean. For this reason, one may consider this peak to represent the boundary between the forward and reverse flowing air.

IV. Part III

We now shift our attention from examining the entire flow domain to examining the region close to the actuator arm. The

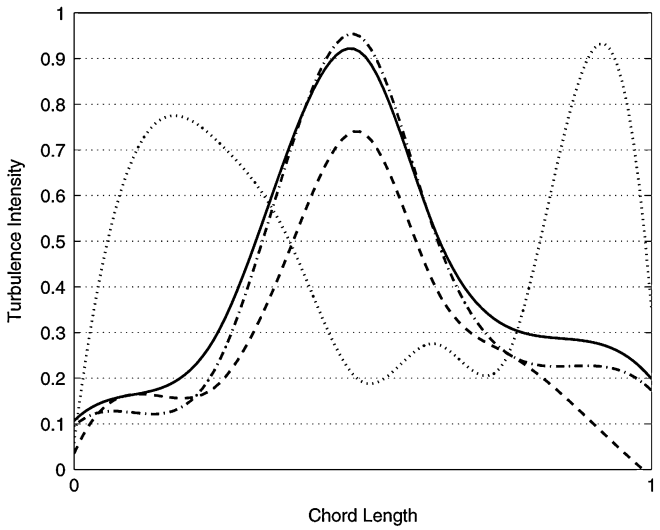

Fig. 19. Turbulence intensity along chord 1. (See Table VIII for legend.)

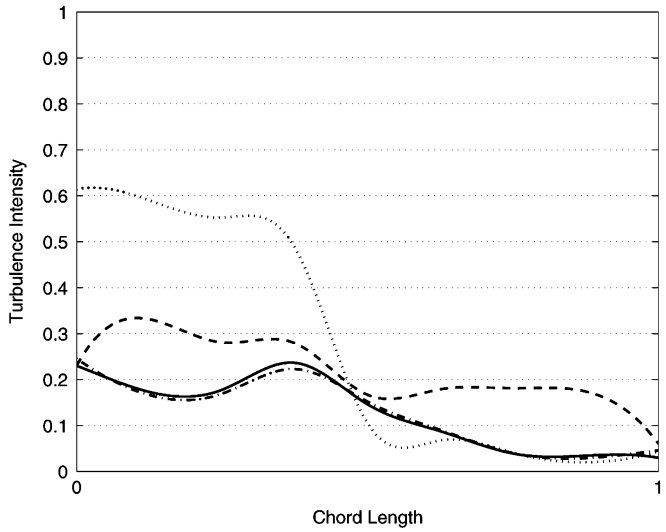

Fig. 20. Turbulence intensity along chord 2. (See Table VIII for legend.)

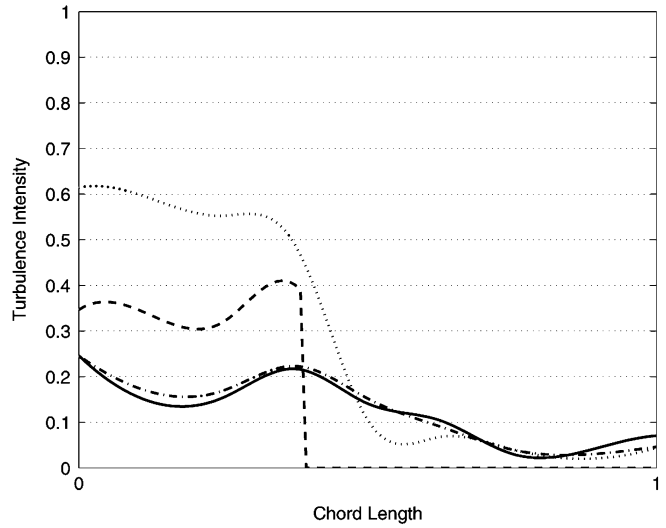

Fig. 21. Turbulence intensity along chord 3. (See Table VIII for legend.)

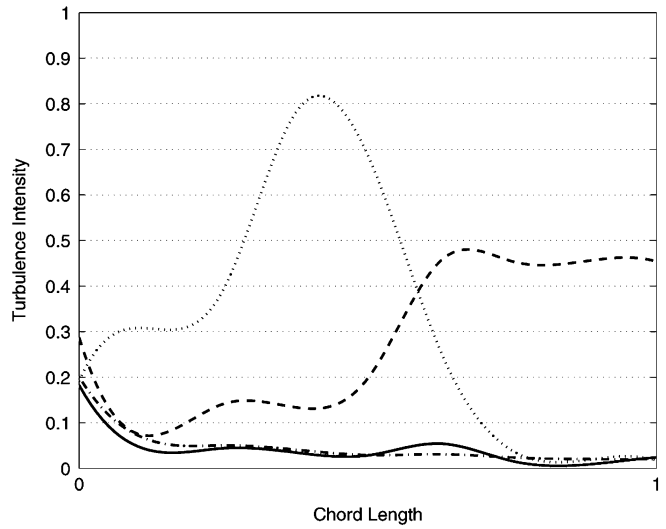

Fig. 22. Turbulence intensity along chord 4. (See Table VIII for legend.)

following results pertain to velocity and pressure data at a few specific points (ranging from 1–32), which are shown in Fig. 23.

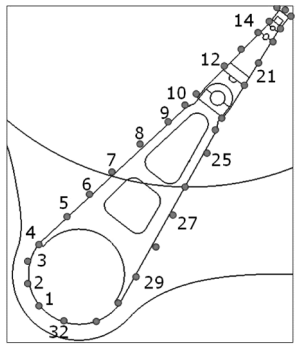

Fig. 23. Location of points along actuator face for which velocity and pressure data is reported.

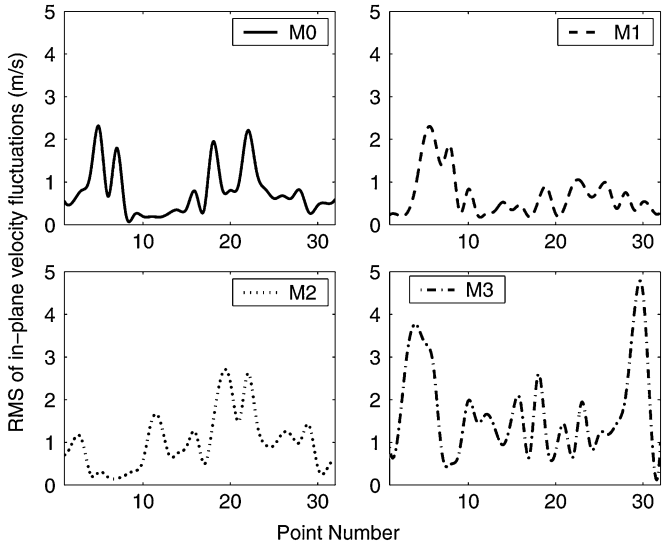

Fig. 24. RMS fluctuation in-plane velocity fluctuations.

These points lie close to the face of the actuator at an axial position which is at the center of the solid structure. For example, points 4–10 are along the centerline of the e-block arm, while 12-22 are along the centerline of the lower suspension. We also note that the frequency spectra reported here using our LES cannot account for the spectra associated with the small scales of motion. LES solves for the large scales by taking into account the energy transfer mechanism between the large and the small scales of motion. However, since there is no explicit representation of the small scales, their contribution to the frequency spectra cannot be obtained.

A. *Velocity Fluctuations*

To begin, we examine the RMS of the in-plane velocity fluctuations. This is plotted in Fig. 24. RMS fluctuations for M0–3 have been plotted on separate subfigures for clarity.

The figure for M0 shows two distinct peaks near points 5–8. These are the fluctuations arising due to the expansion of the shroud just upstream of the e-block arm (see (4) in Fig. 7). Two more peaks in fluctuation are observed: at point 18, due to the eddies at the slider and at points 21–22, due to the eddies from the corner of the base plate.

Comparing this to M1 it appears that M1 is able to dampen the fluctuations near the slider, but the fluctuations near the e-block

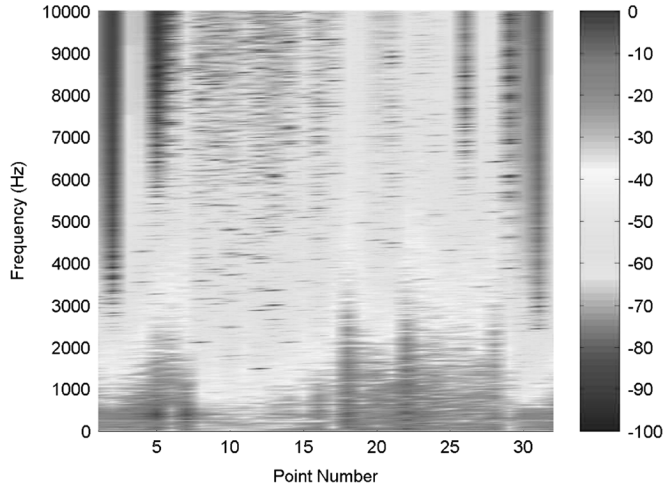

Fig. 25. M0: Frequency spectra of in-plane velocity fluctuations for data points 1–32.

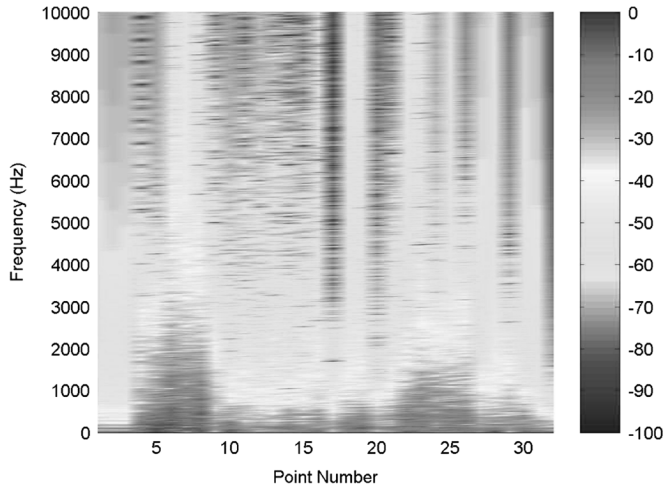

Fig. 26. M1: Frequency spectra of in-plane velocity fluctuations for data points 1–32.

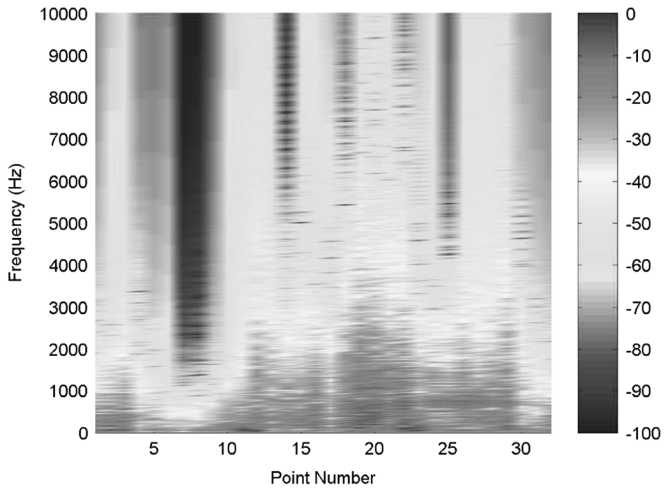

Fig. 27. M2: Frequency spectra of in-plane velocity fluctuations for data points 1–32.

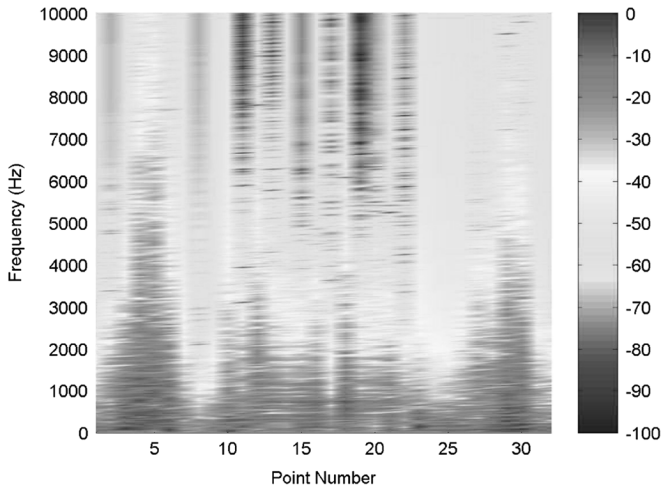

Fig. 28. M3: Frequency spectra of in-plane velocity fluctuations for data points 1–32.

arm actually increase. This is indeed a favorable effect since fluctuations near the e-block arm contribute less to actuator vibrations than fluctuations near the slider. The added fluctuations near the e-block arm are due to the eddies from the trailing edge of the base plate (see (5) in Fig. 8).

M2 displays less fluctuations near the base of the actuator but increased fluctuations near the region of the slider. Finally, M3 shows much higher fluctuations at the base of the actuator (points 1–5 and 29–32) and the base-plate and suspension region (points 10–15) due to the shedding of vortices from the upstream spoiler.

Further insight into the RMS fluctuations can be gained from the frequency spectra of the in-plane velocity at each point. This is plotted for M0–3 (to the same scale) in Figs. 25–28. The coloration of each figure corresponds to decibel amplitude of the spectrum.

Comparing Fig. 26 to Fig. 25, one readily observes that the blocking plate dampens the power in the spectrum at all locations except the base of the e-block arm. However, the spectra do not show significant changes near the suspension using any other modification. In fact, from Fig. 28, it is evident that the presence of the upstream spoiler actually increases the fluctuations surrounding the actuator, especially near the base of the actuator and the leading edge of the suspension. The points 11–23 form the crucial region of the actuator where turbulent fluctuations have the most effect. Clearly, from the spectra in Figs. 25–28 M1 is the most effective in reducing in-plane fluctuations.

Plotted in Fig. 29 are the RMS of the out-of-plane (axial) velocity fluctuations. The plot for M0 shows two significant peaks—one corresponding to the fluctuations arising from the expansion of the shroud, and the other corresponding to the vortex shedding off the slider edge. The trailing edge of the e-block arm (region 24–30) also shows higher axial fluctuations.

In the same figure, one observes that the out-of-plane fluctuations near the slider are reduced by the presence of the blocking plate, they are favorably reduced almost everywhere in M2, but are significantly increased in M3. The upstream spoiler contributes to the significantly high out-of-plane fluctuations near the base of the e-block arm (region 2–5 and 29–32).

Plotted in Figs. 30–33 are the corresponding frequency spectra, which provide more quantitative information regarding the spectral distribution of the out-of-plane velocity fluctuations. Again the spectrum for M1 in Fig. 31 contains lesser

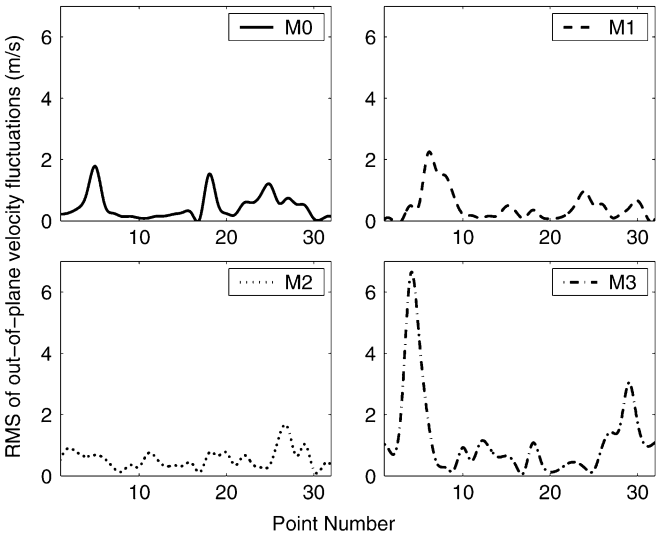

Fig. 29. RMS fluctuation out-of-plane velocity fluctuations.

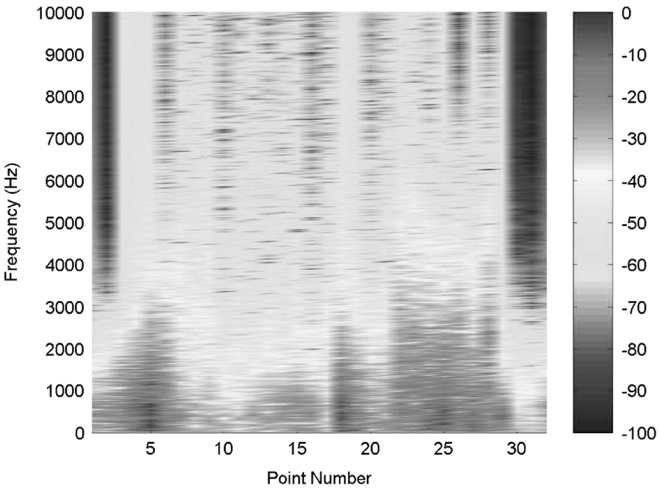

Fig. 30. M0: Frequency spectra of out-of-plane velocity fluctuations for data points 1–32.

power than the spectrum for M0. A common observation from these figures is that, when a modification is used to reduce RMS fluctuations of velocity, higher frequency bands, corresponding to the smaller of the resolved eddies, are damped out. This implies that the energy content of the smaller eddies is reduced by the use of modifications like the blocking plate, while the energy content of the largest eddies, which is determined by the disk spacing and disk speed of rotation, remain relatively unchanged.

Finally, we note the lack of any consistent peak in the frequency spectra of the in-plane or out-of-plane velocity fluctuations. This demonstrates that the vortex shedding process is incoherent (i.e., vortex shedding does not occur preferably at a particular frequency).

B. Pressure Difference Across the Actuator

For hard disk drive actuators it is known that *form drag* due to pressure produces forces 2 orders higher in magnitude than *skin friction* (viscous) drag. Hence, we examine the RMS of pressure fluctuations along the length of the actuator. Fluctuations in

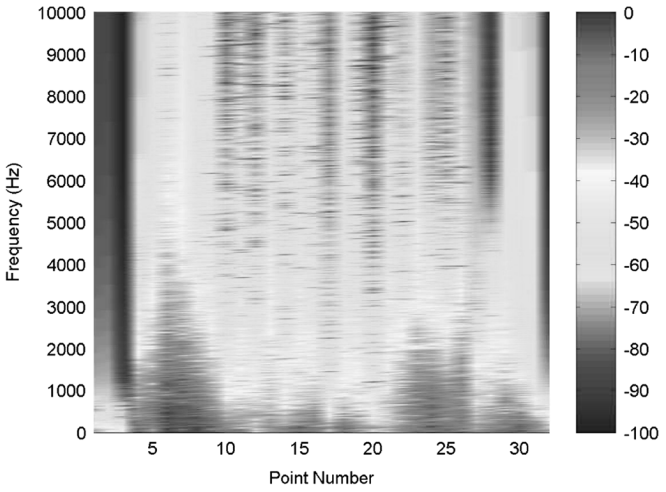

Fig. 31. M1: Frequency Spectra of out-of-plane velocity fluctuations for data points 1–32.

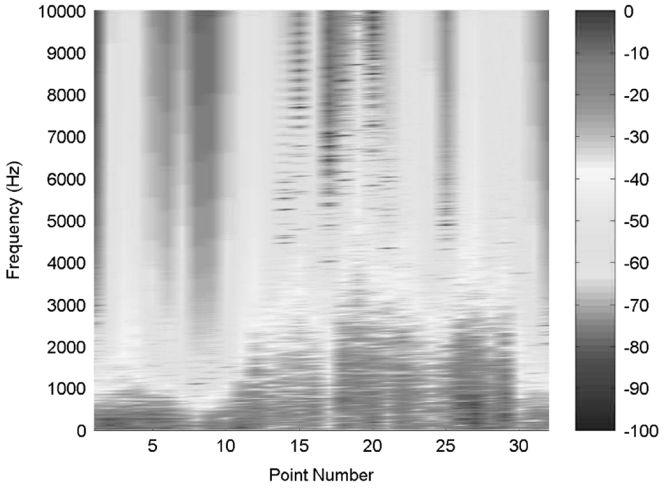

Fig. 32. M2: Frequency Spectra of out-of-plane velocity fluctuations for data points 1–32.

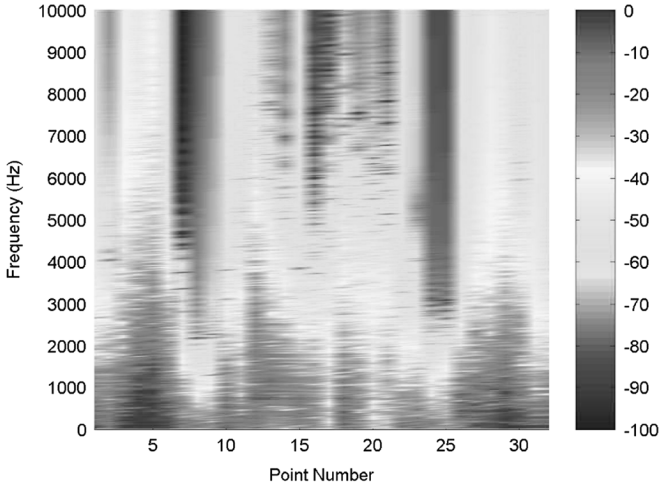

Fig. 33. M3: Frequency spectra of out-of-plane velocity fluctuations for data points 1–32.

pressure at the leading or trailing face of the actuator contribute to it's in-plane motions, while the lesser important out-of-plane

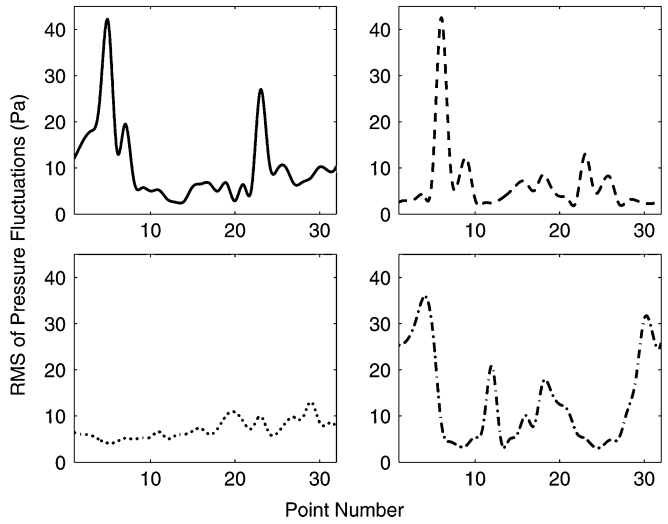

Fig. 34. RMS fluctuations of pressure.

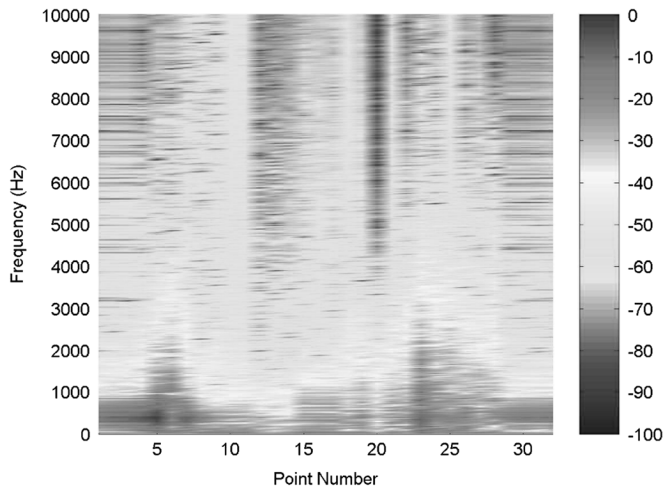

Fig. 35. M0: Frequency spectra of pressure fluctuations for data points 1–32.

pressure fluctuations acting on the top and bottom surfaces of the actuator cause bending in the suspension and e-block arm. We report only the in-plane pressure fluctuations.

Fig. 34 is a plot of the RMS of pressure fluctuation for points 1–32. M0 shows two peaks in the RMS pressure fluctuation, the first due to the eddy separation due to the shroud expansion, while the next is due to the vortex shedding from the edge of the base plate. M1 is effective in reducing the pressure fluctuations due to the vortex shedding from the corner of the base plate. M2 shows much smaller fluctuations near the base of the arm, but the fluctuations are increased near the suspension and base plates. No clear peaks in RMS are observed. Finally, M3 shows significantly larger fluctuations at the base of the actuator and at the location where the turbulent eddies shed from the upstream spoiler impinge on the suspension.

Figs. 35–38 show the frequency spectra of the pressure fluctuations for M0-3. When compared to M0, M1 shows reduced frequency content in the higher frequency bands, indicating that the smaller (resolved) eddies (i.e., eddies of higher frequencies) contribute less to the pressure fluctuations. This is especially important in the region of the suspension (between 14–22). Fig. 37

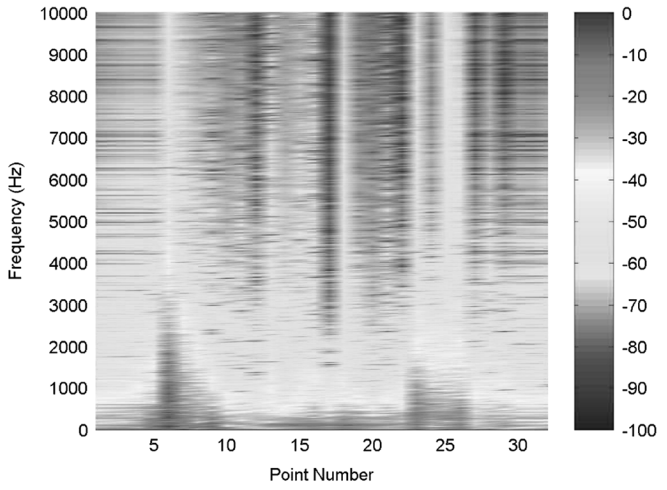

Fig. 36. M1: Frequency spectra of pressure fluctuations for data points 1–32.

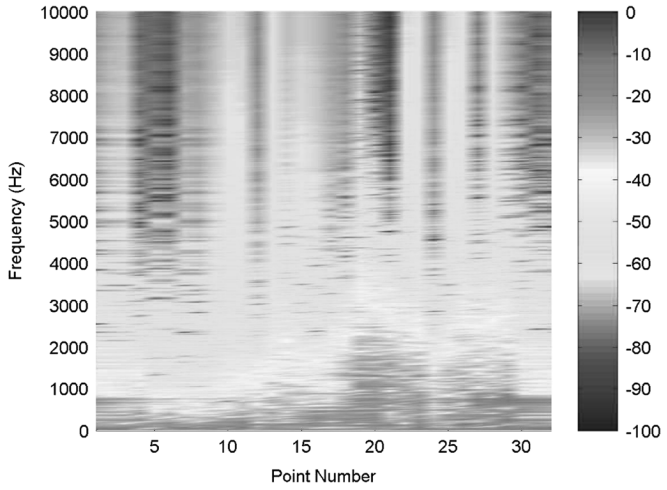

Fig. 37. M2: Frequency spectra of pressure fluctuations for data points 1–32.

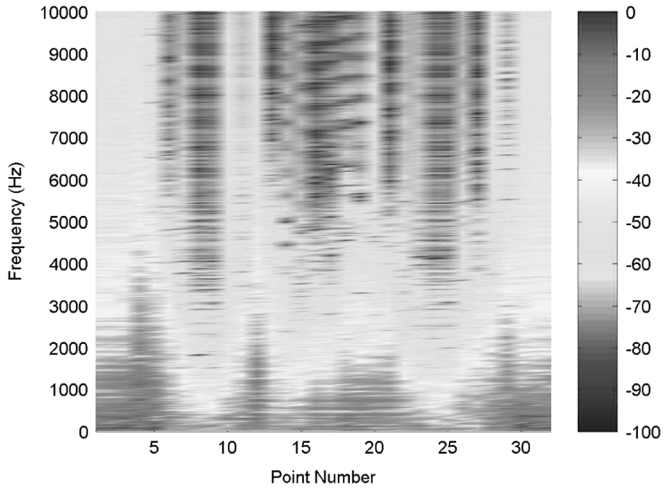

Fig. 38. M3: Frequency spectra of pressure fluctuations for data points 1–32.

shows that with the addition of a downstream spoiler, the frequency content of the spectrum is relatively unchanged, except that the amplitude of the spectrum is overall reduced. This suggests that although the amount of energy in pressure fluctuations

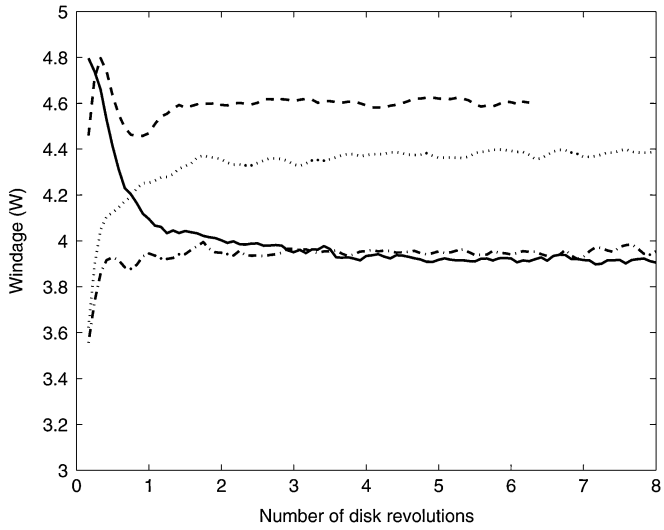

Fig. 39. Windage loss at disks. (See Table VIII for legend.)

has been reduced, the distribution of energy over spatial scales of motion has remained unchanged. Finally, Fig. 38 confirms the fact that the upstream spoiler is ineffective in reducing pressure fluctuations.

C. Windage

It is expected that the cost of using modifications such as M0-3 should not be prohibitively high. Here we report on the *windage loss* calculated as a part of our simulations. Windage is calculated by integrating the shear stress over the disks to determine the power consumed (due to viscous action) by rotating the disks. Windage also represents the total energy input into our computational domain, while the sinks of energy are represented by molecular and sub-grid scale dissipation. Note that our calculations include the viscous loss at the hub, but do not include the viscous loss at the edge (rim) of the disks. It is expected that windage (i.e., energy input) should remain constant over the duration of the simulation. Plotted in Fig. 39 is the time history of the windage calculated as a function of the disk revolutions. One observes that although the initial conditions were inaccurate in predicting the windage, it asymptotes to a constant value in approximately 2 disk revolutions.

One also observes that M1, due to its large blocking plate, consumes the most power, while the windage loss for M2 is also high, given the flow reversal near the hub. This is expected given that the axial velocity gradients are considerably higher for M1 and M2 compared to M0 and M3 leading to higher shear stresses on the disks. The windage losses for M0 and M3 are almost identical.

V. Conclusion

Numerical simulations have revealed several general insights into the flows inside disk drive casings. As the air flows over the actuator, it separates at the leading edge corners. The shear layer formed as a result of this rolls up into vortices which form the wake. The vortex shedding process is devoid of any coherency; it appears to be random as has been confirmed by several other researchers. The turbulent wake is transported by the mean flow of the rotating disks, while is dissipates by viscous action. Additional generation of vorticity takes place at the shroud, where toroidal vortices roll up due to the curvature of the streamlines. The use of the modifications discussed above generally result in additional points of vortex shedding, and depending on where the turbulence intensity is increased in the drive, this additional turbulence may or may not affect the actuator arm. M1 and M2 actually decrease the mean velocity of the flow as is demonstrated in the axial velocity profiles. This reduction in the kinetic energy of the flow (for the same disk rotation speed), causes reduced velocity fluctuations in the wake and in the regions immediately close to the actuator arm. Reiterating, in close proximity to the actuator arm, especially in the region of the base-plate and suspension (see points #11–23 in Fig. 23) M1 has the smallest RMS in-plane and out-of-plane velocity fluctuations. M1 and M2 also have the smallest pressure fluctuations in this region while M3 appears to be a bad candidate based on all the RMS data presented.

We note that pressure-based loading on the actuator accounts for most of the off-track vibrations since pressure drag is 2 orders in magnitude larger than viscous drag. From this metric both M1 and M2 appear to be suitable candidates for reducing flow induced vibrations. However, we note that velocity fluctuations are also responsible for fluctuation of the forces on the actuator, and their effect may not appear directly in the RMS of the pressure fluctuations, which is a second order statistical moment. Changes in the velocity field near the arm causes changes in circulation around the arm, which is linearly related to the loading on the actuator arm. (For the Kutta–Zhukowski theorem, see [29]) Taking this into consideration, it appears that M1 is a better candidate than M2 for reducing flow induced vibrations.

We note that this analysis is not complete in some respects: an accurate representation of the frequency spectra of the flow is lacking. This is because LES was used for the calculation. This can be overcome by using direct numerical simulation (DNS). However, for the complicated geometries investigated here, DNS may remain prohibitively expensive for several years to come. Secondly, LDV measurements of the vibrations of the arm or accurate and reliable dynamic calculations of the response of the actuator arm to the flow, are currently unavailable. The availability of this data will be very useful in validating our results. Finally, in this study, the arm was positioned at the ID position only. The spoiler devices play a different role at different arm positions and the efficacy of these devices across various arm positions is worth investigating.

Acknowledgment

This work was supported by the Computer Mechanics Laboratory (CML) at the University of California, Berkeley.

The authors wish to acknowledge the contribution from Intel Corporation, Hewlett-Packard Corporation, IBM Corporation, and the National Science Foundation Grant EIA-0303575 in making hardware and software available for the CITRIS Cluster which was used in producing these research results.

REFERENCES

[1] R. Wood, J. Miles, and T. Olson, "Recording technologies for terabit per square inch systems," *IEEE Trans. Magn.*, vol. 38, no. 4, pp. 1711–1718, Jul. 2002.

[2] H. Kazemi, "Mathematical modeling of flow-induced vibrations of suspension-head units in hard disk drives," Ph.D. dissertation, Univ. Virginia, Charlottesville, 2004.

[3] E. Lennemann, "Aerodynamic aspects of disk files," *IBM J. Res. Develop.*, pp. 480–488, 1974.

[4] R. Kaneko, S. Oguchi, and K. Hoshiya, "Hydrodynamic characteristics in disk packs for magnetic storage," in *Review of the Electrical Communication Laboratories*, Nippon Telegraph and Telephone Public Corp., Japan, 1977, vol. 25, pp. 1325–1336.

[5] S. D. Abrahamson, J. Eaton, and D. J. Koga, "The flow between shrouded co-rotaing disks," *Phys. Fluids*, vol. 1, no. 2, pp. 241–251, 1989.

[6] J. Girard, S. Abrahamson, and K. Uznanski, "The effect of rotary arms on co-rotating disk fbw," *ASME J. Fluids Eng.*, vol. 117, pp. 259–272, 1995.

[7] H. M. Tzeng and J. A. C. Humphrey, "Corotating disk flow in an axisymmetric enclosure with and without a bluff body," *Int. J. Heat Fluid Flow*, vol. 12, pp. 194–201, 1991.

[8] C. A. Schuler, W. Usry, B. Weber, J. A. C. Humphrey, and R. Grief, "On the flow in the unobstructed space between shrouded corotating disks," *Phys. Fluids A 2*, vol. 10, pp. 1760–1770, 1990.

[9] W. R. Usry, J. A. C. Humphrey, and R. Grief, "Unsteady flow in the unobstructed space between disks corotating in a cylidrical enclosure," *ASME J. Fluids Eng.*, vol. 115, pp. 620–626, 1993.

[10] Y. Yamaguchi, A. A. Talukder, T. Shibuya, and M. Tokuyama, "Air flow around a magnetic head slider suspension and its effects on the slider flying height flictuations," *IEEE Trans. Magn.*, vol. 26, no. 5, pp. 2430–2432, Sep. 1990.

[11] H. Gross, "Off-track vibrations of the read-write heads in hard disk drives," Ph.D. dissertation, Univ. California, Berkeley, 2003.

[12] C. J. Chang, J. A. C. Humphrey, and R. Grief, "Calculation of turbulent convection between corotating disks in axisymmetric enclosures," *Int. J. Heat Mass Transfer*, vol. 33, no. 12, pp. 2701–2720, 1990.

[13] J. A. C. Humphrey, C. A. Schuler, and D. R. Webster, "Unsteady laminar flow between a pair of disks corotating in a fixed cylindrical enclosure," *Phys. Fluids*, vol. 7, no. 6, pp. 1225–1240, 1995.

[14] H. Suzuki and J. A. C. Humphrey, "Flow past large obstructions between corotating disks in fixed cylindrical enclosures," *ASME J. Fluids Eng.*, vol. 119, pp. 499–505, 1997.

[15] I. Iglesias and J. A. C. Humphrey, "Two- and three-dimensional laminar flows between disks co-rotating in a fixed cylindrical enclosure," *Int. J. Numer. Methods Fluids*, vol. 26, pp. 581–603, 1998.

[16] E. Y. K. Ng and Z. Y. Liu, "Prediction of unobstructed flow for Co-rotating multi disk drive in an enclosure," *Int. J. Numer. Methods Fluids*, vol. 35, pp. 519–531, 2001.

[17] H. Shimizu, M. Tokuyama, S. Imai, S. Nakamura, and K. Sakai, "Study of aerodynamic characteristics in hard disk drives by numerical simulation," *IEEE Trans. Magn.*, vol. 37, no. 2, pp. 831–836, Mar. 2001.

[18] N. Tsuda, H. Kobutera, M. Tatewaki, S. Noda, M. Hashiguchi, and T. Maruyama, "Unsteady analysis and experimental verification of the aerodynamic vibration mechanism of HDD arms," *IEEE Trans. Magn.*, vol. 39, no. 2, pp. 819–825, Mar. 2003.

[19] M. Tatewaki, N. Tsuda, and T. Maruyama, "A numerical simulation of unsteady airflow in HDDs," *FUJITSU Set. Tech. J.*, vol. 37, no. 2, pp. 227–235, 2001.

[20] H. Song, M. Damodaran, and Q. Y. Ng, "Simulation of flow field and particle trajectories in hard disk drive enclosures," *High Performance Computation for Engineered Systems (HPCES)*, Jan. 2004.

[21] Y. Hirono, T. Arisaka, N. Nishijima, T. Shimizu, S. Nakamura, and H. Masuda, "Flow-induced vibration reduction in hdd by using a spoiler," *IEEE Trans. Magn.*, vol. 40, no. 4, pp. 3168–3170, Jul. 2004.

[22] S. Nakamura, S. Wakatsuki, T. Haruhide, S. Saegusa, and Y. Hirono, "Flow-induced vibration of head gimbal assembly," *IEEE Trans. Magn.*, vol. 40, no. 4, pp. 3198–3200, Jul. 2004.

[23] S. Deeyienyang and K. Ono, "Suppression of resonance amplitude of disk vibrations by squeeze air bearing plate," *IEEE Trans. Magn.*, vol. 37, no. 2, pp. 820–825, Mar. 2001.

[24] F. Hendriks and A. Chan, "The aerodynamic bypass in hard disk drives," in *Proc. ASME Information Storage and Processing Systems Conf.*, 2005.

[25] M. Germane, U. Piomelli, P. Moin, and W. H. Cabot, "A dynamic sub-grid scale eddy viscosity model," *Phys. Fluids*, vol. A, no. 3, pp. 1760–1765, 1991.

[26] S. Kirpekar and D. B. Bogy, "A comparison of large eddy simulation models for numerical simulation of airflow in hard disk drives," *ASME J. Fluids Eng.*, submitted for publication.

[27] R. Mittal and P. Moin, "Suitability of upwind-biased fi nite difference schemes for large-eddy simulation of turbulent flows," *AIAA J.*, vol. 38, pp. 1415–1417, 1997.

[28] J. P. Van doormaal and G. D. Raithby, "Enhancements of the simple method incompressible fluid flows," *Numer. Heat Transfer*, vol. 7, pp. 147–163, 1984.

[29] P. J. Kundu, *Fluid Mechanics*. New York: Academic, 1990.

Manuscript received April 22, 2005; revised February 22, 2006. Corresponding author: S. Kirpekar (e-mail: kirpekar@newton.berkeley.edu).